Structure of Mesoporous Silica Thin Films Prepared by Contacting $PEO_{106}-PPO_{70}-PEO_{106}$ Films with Vaporized TEOS

Shunsuke Tanaka,*[,†,‡] Michael P. Tate,[§] Norikazu Nishiyama,[†] Korekazu Ueyama,[†] and Hugh W. Hillhouse[§]

Division of Chemical Engineering, Graduate School of Engineering Science, Osaka University, 1-3 Machikaneyama, Toyonaka, Osaka 560-8531 Japan, and School of Chemical Engineering, Purdue University, 480 Stadium Mall Drive, West Lafayette, Indiana 47907

Received June 22, 2006. Revised Manuscript Received September 6, 2006

Highly ordered mesoporous silica thin films have been prepared on silicon substrates by contacting $PEO_{106}-PPO_{70}-PEO_{106}$ (Pluronic F127) triblock copolymer films with hydrolyzed tetraethyl orthosilicate (TEOS) followed by calcination. 2D grazing angle of incidence small angle X-ray scattering (GISAXS) patterns analyzed in the context of the distorted wave Born-approximation (DWBA) show that the films are (111)-oriented and possess rhombohedral symmetry with lattice constants $a = 16.8$ nm and $\alpha = 70°$. Further, high resolution field emission scanning electron microscope (FESEM) observations showed that the films have a lamellar structure supported with periodically arranged pillars. To our knowledge this is the first report of a rhombohedral mesophase obtained using Pluronic F127. Additionally, the pore connectivity in the films here differs from previously reported rhombohedral films. Here the films are capped with a dense layer of silica and appear to not have significant mesoporosity in the direction perpendicular to the substrate. As a result of this structure, after silylation the films have a low relative dielectric constant of ~1.86. In addition, by comparing the X-ray diffraction (XRD) patterns with the GISAXS analysis, we show how using Bragg's law to calculate *d*-spacings from XRD data can significantly underestimate the *d*-spacing. Taking into account the effects of refraction, we report a modified expression of Bragg's law that may be used to recover accurate *d*-spacings from XRD data.

1. Introduction

Porous thin films synthesized by cooperative self-assembly of surfactants with metal oxide precursors have attracted significant attention recently due to their prospects for low dielectric constant films for microelectronics, low refractive index films, photochromic films, and selective sensors.[1−6] Over recent years, a great variety of highly ordered structures have been synthesized, producing many different mesophase topologies, orientations, degrees of order, and framework composition. It should be noted that the final mesostructure depends sensitively on the interfacial curvature at the surfactant/inorganic species boundary.[7,8] This curvature is dependent not only on the initial composition of the reactants, but also on the processing conditions used during self-assembly.[9−11] The common methods of cooperative self-assembly include drop casting, dip coating, and spin coating. However, in this report we use a different approach that employs vapor transport of the silica precursor to control the self-assembly process and to yield a different film structure.[12−15]

The majority of the well-ordered films may be grouped into a handful of space groups. Those space groups include a two-dimensional hexagonal phase *p*6*mm* (which upon uniaxial contraction is characterized by the rectangular plane group *c*2*mm*),[10,11,16,17] a three-dimensional hexagonal phase

* To whom correspondence should be addressed. E-mail: s060002@ipcku.kansai-u.ac.jp and shun_tana@hotmail.com.
† Osaka University.
‡ Current address; Department of Chemical Engineering, Faculty of Engineering, Kansai University, 3-3-35 Yamate-cho, Suita-shi, Osaka 564-8680 Japan.
§ Purdue University.

(1) Schuth, F.; Schmidt, W. *Adv. Mater.* **2002**, *14*, 629.
(2) Konjhodzic, D.; Bretinger, H.; Wilczok, U.; Dreier, A.; Ladenburger, A.; Schmidt, M.; Eich, M.; Marlow, F. *Appl. Phys. A* **2005**, *81*, 425.
(3) Falcaro, P.; Grosso, D.; Amenitsch, H.; Innocenzi, P. *J. Phys. Chem. B* **2004**, *108*, 10942.
(4) Sanchez, C.; Lebeau, B.; Chaput, F.; Boilot, J.-P. *Adv. Mater.* **2003**, *15*, 1969.
(5) Liu, N. G.; Dunphy, D. R.; Atanassov, P.; Bunge, S. D.; Chen, Z.; López, G. P.; Boyle, T. J.; Brinker, C. J. *Nano Lett.* **2004**, *4*, 551.
(6) Bertolo, J. M.; Bearzotti, A.; Falcaro, P.; Traversa, E.; Innocenzi, P. *Sensor Lett.* **2003**, *1*, 64.
(7) Monnier, A.; Schuth, F.; Huo, Q.; Kumar, D.; Margolese, D.; Maxwell, R. S.; Stucky, G. D.; Krishnamurty, M.; Petroff, P.; Firouzi, A.; Janicke, M.; Chmelka, B. F. *Science* **1993**, *261*, 1299.
(8) Huo, Q.; Margolese, D. I.; Ciesla, U.; Demuth, D. G.; Feng, P.; Gier, T. E.; Sieger, P.; Firouzi, A.; Chmelka, B. F.; Schuth, F.; Stucky, G. D. *Chem. Mater.* **1994**, *6*, 1176.
(9) Tate, M. P.; Eggiman, B. W.; Kowalski, J. D.; Hillhouse, H. W. *Langmuir* **2005**, *21*, 10112.
(10) Gibaud, A.; Grosso, D.; Smarsly, B.; Baptiste, A.; Bardeau, J. F.; Babonneau, F.; Doshi, D. A.; Chen, Z.; Brinker, C. J.; Sanchez, C. *J. Phys. Chem. B* **2003**, *107*, 6114.
(11) Cagnol, F.; Grosso, D.; Soler-Illia, G. J. A. A.; Crepaldi, E. L.; Babonneau, F.; Amenitsch, H.; Sanchez, C. *J. Mater. Chem.* **2003**, *13*, 61.
(12) Nishiyama, N.; Tanaka, S.; Egashira, Y.; Oku, Y.; Ueyama, K. *Chem. Mater.* **2003**, *15*, 1006.
(13) Tanaka, S.; Nishiyama, N.; Oku, Y.; Egashira, Y.; Ueyama, K. *J. Am. Chem. Soc.* **2004**, *126*, 4854.
(14) Tanaka, S.; Nishiyama, N.; Hayashi, Y.; Egashira, Y.; Ueyama, K. *Chem. Lett.* **2004**, *33*, 1408.
(15) Tanaka, S.; Maruo, T.; Nishiyama, N.; Egashira, Y.; Ueyama, K. *Chem. Lett.* **2005**, *34*, 1148.
(16) Gibaud, A.; Bardeau, J.-F.; Dutreilh-Colas, M.; Bellour, M.; Balasubramanian, V. V.; Robert, A.; Mehdi, A.; Reye, C.; Corriu, R. J. *J. Mater. Chem.* **2004**, *14*, 1854.

10.1021/cm0614463 CCC: $33.50
Published on Web 10/18/2006

$p6_3/mmc$,[10,18,19] a primitive cubic phase $Pm3n$,[10,11] a body-centered cubic phase $Im3m$ (which upon uniaxial contraction is characterized by the orthorhombic plane group $Fmmm$),[3,20] a body-centered tetragonal phase $I4/mmm$,[20] a gyroid-based cubic phase $Ia3d$,[21] and a rhombohedral phase $R\bar{3}m$.[9,17,22] The space group symmetry describes the periodicity of the mesostructure, which is well-ordered and has a narrow pore size distribution reminiscent of microporous zeolite crystals, but with mesopore dimensions.

The most common tool used to identify structure is X-ray diffraction (XRD) (widely available and typically used for powders), though advanced evaluation procedures were currently applied to determine the structural parameters of mesostructured silica films using small-angle X-ray scattering in symmetric reflection.[23−25] Although the self-assembled mesostructures are not crystalline, the diffraction occurs due to the periodic contrast in electron density between the amorphous framework and pores (or surfactant regions). However, these films generally show only a few peaks in XRD patterns due to the one-dimensional scan of reciprocal space in traditional one-dimensional diffractometers. Additionally, due to the small diffraction angles involved (commonly less than 2° 2θ), there arises the need to correct the Bragg peak location for the effects of refraction at the air/film interface. The limited number of observed peaks, combined with refraction effects, make identification of the space group, orientation, and lattice constants very difficult with standard XRD. To remedy this, two-dimensional small-angle X-ray scattering (SAXS) techniques may be used to determine the mesostructure. Two-dimensional SAXS patterns collected at small angles of incidence to the film surface allow the Ewald sphere to slice through reciprocal space in a way that bisects the ringlike patterns that result from films oriented with respect to the substrate normal but are free to rotate in the plane of the substrate.[26] When this technique is performed using very thin substrates and at moderately low angles of incidence (~2°), the diffracted beams are transmitted through the substrate and the technique is called 2D transmission SAXS. Even for the thinnest substrates, data collection times may be large for laboratory instruments. However, if the angle of incidence is decreased such that the diffracted beams never pass through the substrate (angles of incidence typically less than 0.5°), one can collect data very rapidly, even on laboratory sources. This technique is called grazing angle of incidence SAXS (GISAXS) and can reveal most of the features of reciprocal space.[27] The effective sample volume for scattering becomes large at grazing incidence angles, resulting in strong scattering patterns from layers only a few hundred nanometers thick.

In this report, we identify the topology, order, and orientation of mesoporous silica thin films prepared by vapor-phase synthesis.[12−15] The symmetry and lattice constants of the films were determined by the combination of GISAXS with simulations[27] based on the distorted-wave Born approximation[28−35] to interpret the results. The mesopore topology is identified by field emission scanning electron microscope (FESEM) and transmission electron microscope (TEM) measurements. Additionally, since most researchers have access to XRD instruments, we compare the Bragg peak positions observed by XRD with those observed by GISAXS. The comparison highlights the need to correct the XRD data for X-ray refraction at the air/film interface as these effects are not negligible and corrections are necessary to make accurate quantitative analysis of the ordered mesoporous films with large lattice constants.

2. Experimental Section

A template precursor solution was prepared by dissolving 1.89 g of Pluronic F127, a nonionic $PEO_{106}-PPO_{70}-PEO_{106}$ copolymer, in 23 g of ethanol and 9 g of deionized water. A 0.5-mL portion of this solution was spin-coated on a silicon substrate (2.5 × 2.5 cm piece) at a rotating speed of 4000 rpm for 1 min. The resultant polymer film was placed in a sealed 60-mL vessel along with a separate (in 0.5 mL Teflon vessel) small amount of tetraethylorthosilicate (TEOS) and hydrochloric acid (5 N HCl). The vessel was then placed in an oven at 90 °C for 1 h to infiltrate the polymer film with TEOS, HCl, and water. Afterward, removal of the template was conducted by calcination at 400 °C for 5 h with a heating and cooling ramp of 1 °C/min.

Most of the GISAXS patterns were collected from films using high-intensity synchrotron radiation on beamline 8-ID-E at Advanced Photon Source (wavelength 0.1631 nm, angle of incidence $\alpha_i = 0.22°$), Argonne National Laboratory. A schematic of the geometry of the GISAXS setup is shown in Figure 1a. The substrate was positioned vertically and an elongated beam stop was used to attenuate the scattering along the specular plane. The 2D GISAXS data are plotted as a function of $2\theta_f$ and α_f, the in-plane and out-of-plane exit angles, respectively, with an arbitrary intensity scale. Diffraction spot patterns were simulated using NANOCELL,[27] a Mathematica-based program for predicting SAXS and GISAXS peak positions at any angle of incidence above the critical angle α_c. This simulation code uses the distorted-wave Born approximation (DWBA) to account for reflection and refraction effects.

(17) Eggiman, B. W.; Tate, M. P.; Hillhouse, H. W. *Chem. Mater.* **2006**, *18*, 723.
(18) Besson, S.; Ricolleau, C.; Gacoin, T.; Jacquiod, C.; Boilot, J.-P. *J. Phys. Chem. B* **2000**, *104*, 12095.
(19) Sophie, B. A.; Gacoin, T.; Jacquiod, C.; Ricolleau, C.; Babonneau, D.; Boilot, J.-P. *J. Mater. Chem.* **2000**, *10*, 1331.
(20) Innocenzi, P.; Malfatti, L.; Kidchob, T.; Falcaro, P.; Costacurta, S.; Guglielmi, M.; Mattei, G.; Belloc, V.; Amenitschd, H. *J. Synchrotron Radiat.* **2005**, *12*, 734.
(21) Hayward, R. C.; Alberius, P. C. A.; Kramer, E. J.; Chmelka, B. F. *Langmuir* **2004**, *20*, 5998.
(22) Naik, S. P.; Yokoi, T.; Fan, W.; Sasaki, Y.; Wei, T.-C.; Hillhouse, H. W.; Okubo, T. *J. Phys. Chem. B* **2006**, *110*, 9751.
(23) Ruland, W.; Smarsly, B. *J. Appl. Crystallogr.* **2004**, *37*, 575.
(24) Ruland, W.; Smarsly, B. *J. Appl. Crystallogr.* **2005**, *38*, 78.
(25) Smarsly, B.; Gibaud, A.; Ruland, W.; Sturmayr, D.; Brinker, C. J. *Langmuir* **2005**, *21*, 3858.
(26) Klotz, M.; Albouy, P. A.; Ayral, A.; Menager, C.; Grosso, D.; Van der Lee, A.; Cabuil, V.; Babonneau, F.; Guizard, C. *Chem. Mater.* **2000**, *12*, 1721.
(27) Tate, M. P.; Urade, V. N.; Kowalski, J. D.; Wei, T.-C.; Hamilton, B. D.; Eggiman, B. W.; Hillhouse, H. W. *J. Phys. Chem. B* **2006**, *110*, 9882.
(28) Vineyard, G. *Phys. Rev. B* **1982**, *26*, 4146.
(29) Wagner, H.; Dietrich, S. *Phys. Rev. Lett.* **1983**, *51*, 1469.
(30) Sinha, S. K.; Sirota, E. B.; Garoff, S.; Stanley, H. B. *Phys. Rev. B* **1988**, *38*, 2297.
(31) Rauscher, M.; Salditt, T.; Spohn, H. *Phys. Rev. B* **1995**, *52*, 16855.
(32) Holy, V.; Kubena, J.; Ohlidal, I.; Lischka, K.; Plotz, W. *Phys. Rev. B* **1993**, *47*, 15896.
(33) Holy, V.; Baumbach, T. *Phys. Rev. B* **1994**, *49*, 10668.
(34) Lazzari, R. *J. Appl. Crystallogr.* **2002**, *35*, 406.
(35) Lee, B.; Park, I.; Yoon, J.; Park, S.; Kim, J.; Kim, K. W.; Chang, T.; Ree, M. *Macromolecules* **2005**, *38*, 4311.

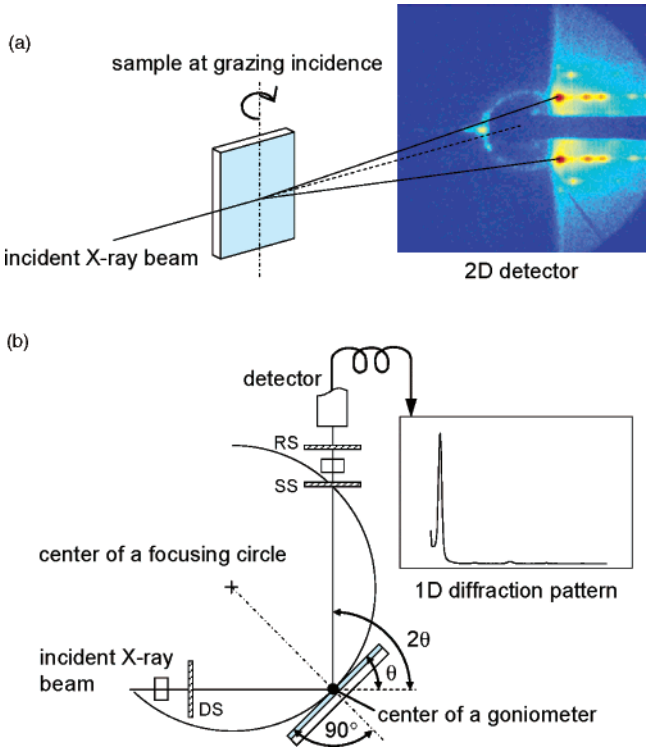

Figure 1. Schematic representations for (a) 2D GISAXS setup and (b) XRD with $\theta-\theta$ Bragg−Brentano geometry.

XRD patterns were recorded on a Scintag X2 $\theta-\theta$ diffractometer using Cu Kα radiation with 1.5418 Å. A schematic of the XRD diffractometer is shown in Figure 1b. The copper anode was operated at a voltage of 33 kV and a current of 17 mA. Beam aperture was manually adjusted using a divergence slit (DS) for the beam source and scattering slit (SS) and receiving slit (RS) for the detector to reduce background scattering and limit the beam divergence. Diffraction patterns were collected over the range of 0.6−4° 2θ at a scan rate of 0.01° 2θ/min and a step size of 0.01°.

FESEM measurements were carried out on a Hitachi S-5000L instrument at an accelerating voltage of 21 kV, without any surface coating of the film samples. TEM images of a calcined mesoporous silica film were recorded on a Hitachi H9000 instrument at an acceleration voltage of 300 kV.

The dielectric constant of the films was measured at room temperature with a Solatron SI 1260 impedance analyzer in a frequency range of 10 kHz−1 MHz. Platinum electrodes were prepared by sputter deposition, the area of which is 7.85×10^{-3} cm^2.

3. Results and Discussion

Identification of Structure and Topology. The structure and orientation of the calcined thin film were characterized by 2D GISAXS shown in Figure 2. The large number of peaks in the 2D pattern indicates that the film is highly ordered and oriented. Additionally, from the 2D pattern the critical angle (α_c) is easily identified by the diffuse intensity maximum along a constant (α_f); in this case $\alpha_c = 0.180°$. To solve for the space group, orientation, and lattice constants, the X-ray scattering patterns for the calcined films were compared to a wide range of simulated GISAXS patterns using NANOCELL. The best fits were obtained with a rhombohedral structure (space group $R\bar{3}m$) oriented with the (111) plane parallel to the substrate. The lattice constants for the film were determined to be $a = 16.8$ nm and $\alpha = 70°$. The order and orientation of the mesostructure determined by the analysis is shown schematically in Figure 3. In addition to the peak positions, additional information is obtained by observing the diffuse features of the pattern. The streaking of the Bragg peaks normal to the substrate suggests that something interrupts the rhombohedral symmetry in the vertical direction, causing the $R\bar{3}m$ domain size to be small in that direction.[9]

If the absorption of X-ray is ignored, the total reflection occurs up to the critical angle α_c given by[36]

$$\alpha_c = \sqrt{2\delta} = 1.639 \times 10^{-2}\sqrt{\rho}\lambda \qquad (1)$$

where α_c is in radians, ρ is the density of the film in g/cm^3, and λ is the wavelength in nm. Conversely, if the critical angle is known, the density of the film may be calculated. That is the case here, where from the GISAXS data the critical angle is known, and thus the average density is calculated to be 1.38 g/cm^3. If the silica framework is assumed to have a density of 2.2, then the mesoporosity of the film can be estimated to be 37.2%.

FESEM images (Figure 4) show the structure in real space and confirm the unique architecture observed in these films. The lattice constants observed from FESEM images are in good agreement with those calculated by fitting the GISAXS pattern. A highly ordered pattern of cagelike pores was observed in the TEM micrograph taken perpendicular to the film surface, shown in Figure 5a. This nearly hexagonal closed packed pattern supports the conclusion that the (111) planes are parallel to the substrate. Cagelike mesopores were on average roughly aligned along the (111) direction. The structure was further elucidated by the TEM observation in the direction perpendicular to the film surface.

Tate and co-workers[9,17] and Naik et al.[22] have also recently reported $R\bar{3}m$-structured silica films using $PEO_{20}-PPO_{70}-PEO_{20}$ (Pluronic P123) or cetyltrimethylammonium bromide in the presence of 1,3,5-triisopropylbenzene, respectively. For the P123 films synthesized by dip-coating, FESEM data show that the top most layer of cages are open to the region above the film. This is in contrast to the films obtained in this study, which are identical in space group and orientation, but the pores are not open to the vapor phase. The top-surface of the film terminates with a dense silica layer (see Figure 5b). When the top layers are peeled off, stubs of the periodically arranged silica pillars are observed (see Figure 5c). In many regions, such as that imaged in Figure 5d, the film appears to have a unique layered structure where the layers are connected by an ordered array of pillars. The structure of the film is homogeneous through the thickness of the film. This pore connectivity may be attributed to the formation process of the ordered mesostructure. The lamellar structure formed in the early stage of the TEOS infiltration and then pillars are formed with increasing concentration of TEOS in the film.[13] This results in a film with no interconnection of pores through the thickness of the film. To the best of our knowledge, this is the first report of such an $R\bar{3}m$

(36) Guinier, A. *X-Ray Diffraction*; W. H. Freeman and Co.: San Francisco, 1963.

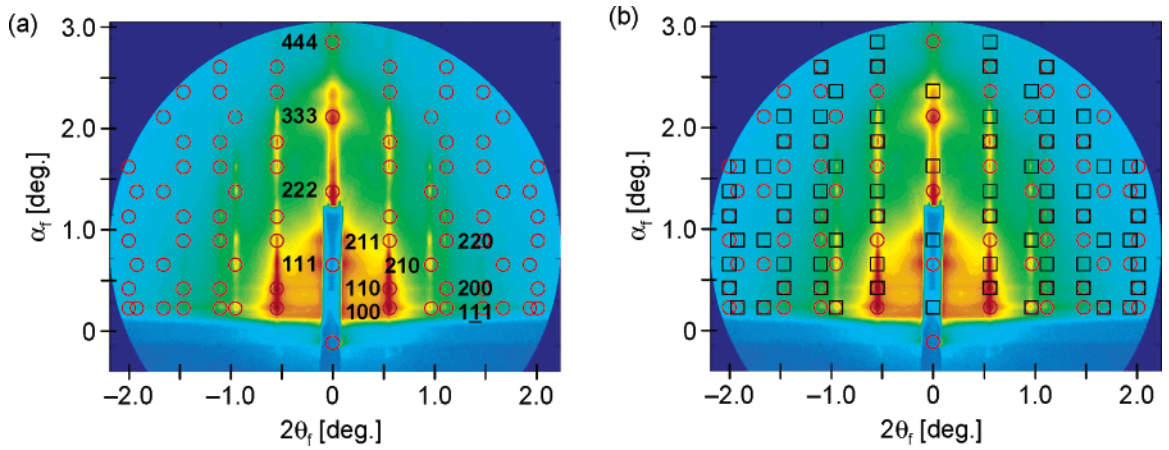

Figure 2. GISAXS patterns collected from synchrotron source ($\alpha_i = 0.22°$) for mesostructured silica thin film with overlays showing simulated spot patterns using DWBA: (a) only transmitted spots shown and (b) both transmitted and reflected spots shown. In each part the circles indicate transmitted Bragg spots while the squares indicate reflected Bragg spots.

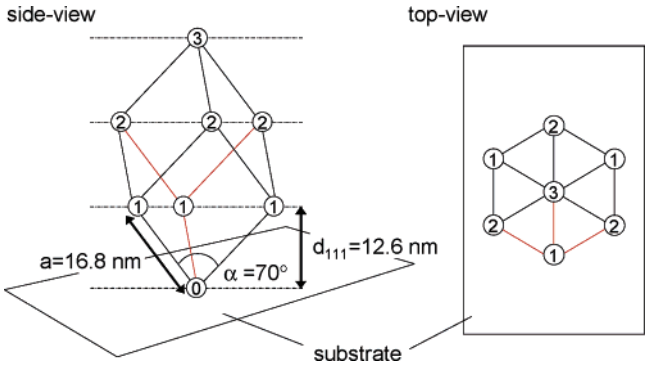

Figure 3. Schematic showing the order and orientation of the $R\bar{3}m$ structure with respect to the substrate.

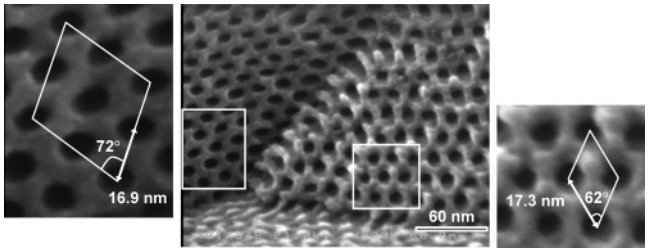

Figure 4. FE-SEM image of the cross-section of the ordered mesoporous silica thin film.

structure and additionally the first to use Pluronic F127 as the templating agent for this phase.

Dielectric Properties of the Films. Mesostructured polymer/silica was prepared on the conductive substrate, and then vapor infiltration treatment using trimethylethoxysilane was conducted at 150 °C for 3 h to introduce trimethylsilyl groups into the silica wall.[37] In the vapor infiltration technique, organic groups can be incorporated in the films without a reduction in pore size. The polymer template was removed by extraction after thermal treatment at 150 °C for 24 h. Then the mesoporous silica films were further dehydroxylated by the silylation with trimethylchlorosilane at 150 °C for 2 h. Removal of the template and replacement of the residual silanol groups by the methylsilyl groups were confirmed by the Fourier transform infrared spectroscopy.

(37) Tanaka, S.; Kaihara, J.; Nishiyama, N.; Oku, Y.; Egashira, Y.; Ueyama, K. *Langmuir* **2004**, *20*, 3780.

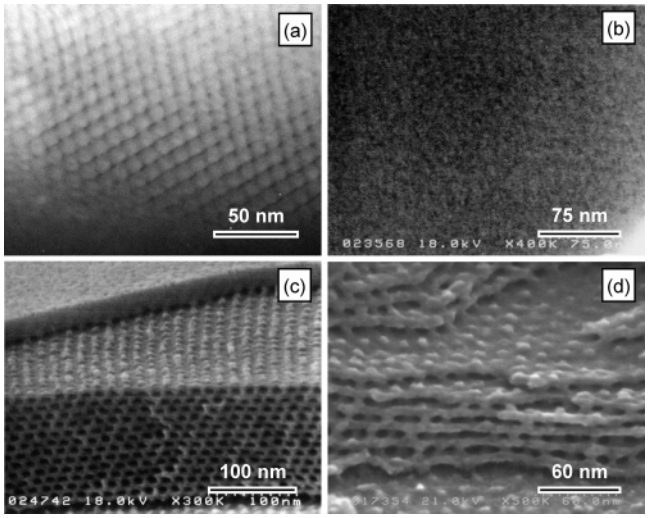

Figure 5. (a) Top-view TEM micrograph of the ordered mesoporous silica thin film. (b) Top-view FESEM image of the film surface. (c) FESEM image of the film where the top silica layer was peeled off. (d) FESEM image of the film where the silica layers were peeled off.

The dielectric constant of the films was ~1.86, which was lower than that of dense silica because of the higher mesoporosity and hydrophobicity of the films. Additionally, the layered structure with pillars are of advantage for microelectronic low dielectric constant films, because the silica layer does not have pore accessibility and the top surface plays a role as passivating film.

Comparison of XRD and GISAXS Data. Figure 6 shows the XRD pattern, recorded $\theta-\theta$ Bragg−Brentano scanning geometry, for the (111)-oriented $R\bar{3}m$-structured film with $a = 16.8$ nm and $\alpha = 70°$. The XRD pattern shows a series of Bragg diffraction peaks. The *d*-spacing from the first peak is calculated to be 11.3 nm using the well-known Bragg's equation without taking the refraction event into consideration:

$$d = \frac{\lambda}{2\sin(2\theta_{obs}/2)} \qquad (2)$$

where, θ_{obs} is used to indicate the Bragg diffraction peak position observed in the XRD pattern. Given the phase and orientation determined by GISAXS, this peak can be indexed

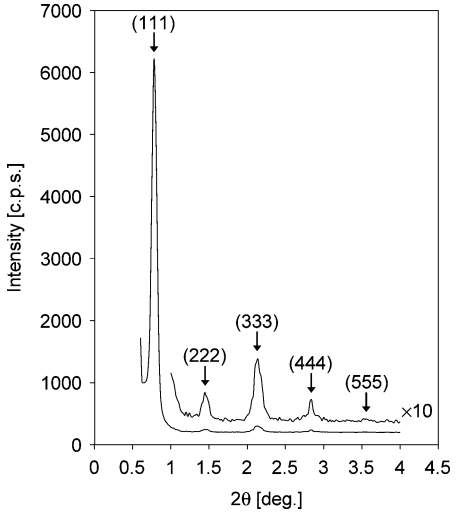

Figure 6. XRD pattern of (111)-oriented rhombohedral $R\bar{3}m$-structured silica film without (*h*00), (*hk*0), and (*hkl*) ($h \neq k \neq l$) Bragg diffraction peaks.

Table 1. Bragg Diffraction Peak Positions and Lattice Spacings Calculated by the Traditional and Modified Bragg's Equation, and *d*-Spacing Formula Using the Lattice Constants from GISAXS/NANOCELL

	$2\theta_{obs}$ (XRD), deg	d_{obs},[a] nm	d_{GN},[b] nm	d_{act}[c] = d_{MB},[d] nm
(111)	0.78	11.3	12.6	12.6
(222)	1.45	6.09	6.29	6.29
(333)	2.13	4.15	4.20	4.20
(444)	2.83	3.12	3.15	3.15
(555)	3.53	2.50	2.52	2.52

[a] Calculated by the traditional Bragg's equation (eq 2) using θ_{obs} (the Bragg diffraction peak position observed in XRD pattern). [b] Calculated by the *d*-spacing formula using lattice constants obtained from GISAXS/NANOCELL, eq 3. [c] Calculated by the traditional Bragg's equation (eq 2) using θ_{act}. [d] Calculated by the modified Bragg's equation (eq 7) using the critical angle 0.171°.

as the (111), with the subsequent peaks indexed as the (222), (333), etc. However, the d_{111} calculated from GISAXS analysis is 12.6 nm. That spacing is obtained from the lattice constants obtained using the DWBA and the following geometric formula for the rhombohedral unit cell:

$$d = \sqrt{\frac{a^2(1 - 3\cos^2\alpha + 2\cos^3\alpha)}{(h^2 + k^2 + l^2)\sin^2\alpha + 2(hk + kl + lh)(\cos^2\alpha - \cos\alpha)}} \quad (3)$$

where *h*, *k*, and *l* are Miller indices of the Bragg peaks. However, it is observed that the subsequent peaks are not evenly spaced as may be expected. Each d_{obs} shown in Table 1 is calculated by the well-known Bragg's equation, eq 2. Comparing d_{obs} to the calculation based on the lattice constants obtained from GISAXS (d_{GN}), the *d*-spacings calculated from XRD (d_{obs}) underestimate the true *d*-spacings.

Care was taken to correct for possible sources of error in the collection of the XRD data. Sources of error in the Bragg peak position may include (1) error in the zero position of the 2θ axis, (2) vertical displacement of the sample, (3) specimen transparency, (4) sample flatness, and (5) vertical divergence. The effects of errors 3−5 have been simulated

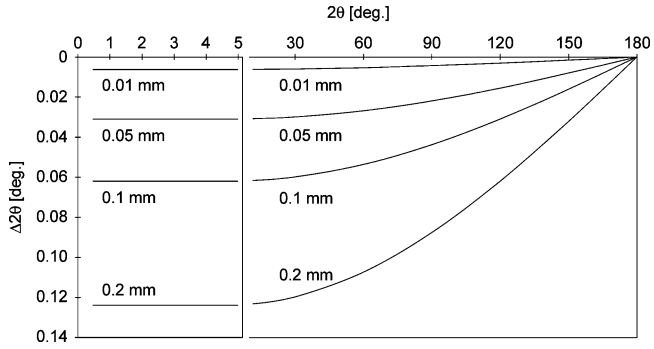

Figure 7. The error of 2θ due to the vertical displacement of the sample.

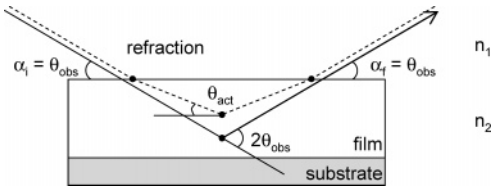

Figure 8. Overview of refraction events upon the interface between air and film.

and are typically negligible in the current model.[38] This leaves as possible sources of error the effects of 1 and 2, which can be accounted for by the following:

$$\Delta 2\theta = \Delta 2\Theta_0 - 2S\cos\theta/R \quad (4)$$

where $\Delta 2\Theta_0$ is the error in the zero 2θ position, *S* is the specimen displacement, and *R* is the goniometer radius (=185 mm). Note that the value of second term in eq 4 becomes nearly constant at low 2θ angle (see Figure 7). If the peak shifts arise from the effects of principal sources 1 and 2 of the error, all the peaks should be shifted along 2θ by a constant value. The angular shifts of the diffraction peaks, observed in the XRD pattern of the mesoporous silica thin films, were not explained by the effects of principal sources 1 and 2 of the error in the peak locations.

However, these shifts may be understood by considering refraction effects. When X-rays enter a medium in which the refractive index is different than that of which the X-rays had just left (such as the air/film interface of the films), a refraction event occurs. Consequently, the direction of the incident and exit X-ray beams within the film are different than those outside the film (as shown in Figure 8). This has the effect of shifting all the observed Bragg diffraction peaks to higher angle than those indicated by Bragg's law. To calculate the direction of both the incident and diffracted beams inside the film, the standard law of refraction is used. When the beam directions are defined according to Figure 8, the law of refraction is written as[28]

$$n_1\cos\theta_1 = n_2\cos\theta_2 \quad (5)$$

where n_1 and n_2 are the refractive index of X-ray for vacuum (air: $n_1 = 1$) and film, respectively. The α_c, the critical angle for the air/film interface, may then be expressed as

$$\cos\alpha_c = n_2 \quad (6)$$

(38) Ida, T.; Kimura, K. *J. Appl. Crystallogr.* **1999**, *32*, 982.

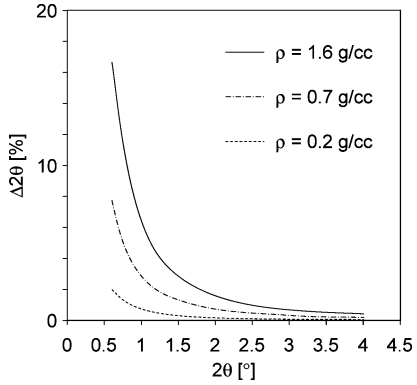

Figure 9. The deviation of 2θ due to the refraction event.

When $n_1 > n_2$ (as is the case for most materials when using X-rays), the angle of refraction θ_{act} becomes smaller than the angle of incidence θ_{obs} (Figure 8). The Bragg equation can then be expressed using θ_{act} as

$$d = \frac{\lambda}{2 \sin\{\cos^{-1}(\cos \theta_{obs}/\cos \alpha_c)\}} \quad (7)$$

The *d*-spacings (d_{MB}) calculated from the modified Bragg's equation, eq 7, using $\alpha_c = 0.171°$ now match spacings obtained from GISAXS quite well. The critical angle α_c, where the λ is 0.1542 nm (Cu Kα radiation), was estimated to be 0.171° from the eq 1. Note there can be an error of 10% in the *d*-spacing obtained if one uses the Bragg equation without correcting for refraction. Particularly for films that are not oriented and show more than one family of diffraction planes in XRD, this error could cause misidentification of the phase.

To further highlight the need to account for refractive effects at small angles, the error introduced by neglecting the refraction effect in XRD is shown in Figure 9 for several different film densities (this affects the critical angle). To determine the magnitude of the deviation, the critical angle α_c for total reflection is determined from the density of film by eq 1. At higher angles (above 3° or 4° 2θ) the shift can be neglected except in high accuracy measurements. However, for ordered mesostructured materials formed via self-assembly of surfactants that have large lattice constants (~20 nm) such effects cannot be neglected.

4. Conclusions

Highly ordered mesoporous silica thin films have been synthesized by vapor-phase synthesis and characterized using the combination of GISAXS, FESEM, and TEM measurements. The structure of the films was indexed with the rhombohedral space group $R\bar{3}m$ and found to be oriented through the thickness of the film with the (111) direction perpendicular to the substrate. The diffraction spot positions in GISAXS patterns are predicted accurately by NANOCELL code using the DWBA. Further, it was found that refraction effects significantly shift the diffraction peak positions to higher observed angles observed when using a conventional $\theta-\theta$ diffractometer. As a result, the *d*-spacing is underestimated for ordered mesoporous films with large lattice constants in standard XRD measurements. Additionally, the use of GISAXS/NANOCELL has enabled determination of the mesophase symmetry and order in oriented mesoporous silica films, which is not possible from XRD alone. Finally, when the Bragg's equation is modified to allow for the refraction at the air/film interface, correct *d*-spacing values are obtained.

Acknowledgment. The authors wish to acknowledge use of the NSF funded facility for in-situ X-ray Scattering from Nanomaterials and Catalysts (MRI program award 0321118-CTS) and the use of the Advanced Photon Source supported by the U.S. Department of Energy, Office of Science, Office of Basic Energy Sciences, under Contract No. W-31-109-ENG-38. The authors gratefully acknowledge the assistance of the GHAS laboratory and Mr. M. Kawashima at Osaka University with the FE-SEM measurements. The authors wish to thank Prof. H. Mori and Dr. T. Sakata at Osaka University (Research Center for Ultra-High Voltage Electron Microscopy) for TEM measurements. S. Tanaka acknowledges the Japan Society for the Promotion of Science (JSPS) Research Fellowships.

CM0614463